

Pilot-Based SFO Estimation for Bistatic Integrated Sensing and Communication

Lucas Giroto de Oliveira, *Graduate Student Member, IEEE*, Yueheng Li, Silvio Mandelli, *Member, IEEE*, David Brunner, Marcus Henninger, *Member, IEEE*, Xiang Wan, *Senior Member, IEEE*, Tie Jun Cui, *Fellow, IEEE*, Thomas Zwick, *Fellow, IEEE*, and Benjamin Nuss, *Senior Member, IEEE*

Abstract—Enabling bistatic radar sensing within the context of integrated sensing and communication (ISAC) for future sixth generation mobile networks demands strict synchronization accuracy, which is particularly challenging to be achieved with over-the-air synchronization. Existing algorithms handle time and frequency offsets adequately, but provide insufficiently accurate sampling frequency offset (SFO) estimates that result in degradation of obtained radar images in the form of signal-to-noise ratio loss and migration of range and Doppler shift. This article introduces an SFO estimation algorithm named tilt inference of time offset (TITO) for orthogonal frequency-division multiplexing (OFDM)-based ISAC. Using available pilot subcarriers, TITO obtains channel impulse response estimates and extracts information on the SFO-induced delay migration to a dominant reference path with constant range, Doppler shift, and angle between transmit and receive ISAC nodes. TITO then adaptively selects the delay estimates that are only negligibly impaired by SFO-induced intersymbol interference, ultimately employing them to estimate the SFO. Assuming a scenario without a direct line-of-sight (LoS) between the aforementioned transmitting and receiving ISAC nodes, a system concept with a relay reflective intelligent surface (RIS) is used to create the aforementioned reference path is proposed. Besides a mathematical derivation of accuracy bounds, simulation and measurements at 26.2 GHz are presented to demonstrate TITO’s superiority over existing methods in terms of SFO estimation accuracy and robustness.

Index Terms—6G, bistatic sensing, integrated sensing and communication (ISAC), orthogonal frequency-division multiplexing (OFDM), reflective intelligent surface (RIS), synchronization.

I. INTRODUCTION

SIXTH generation (6G) networks are expected to be introduced with the aim of not only increasing connection rate and its reliability, but also enabling a multitude of functionalities beyond data communication [1]. Among the

latter, integrated sensing and communication (ISAC) [2]–[5] comes as a disruptive feature with the potential of turning cellular networks into perceptive mobile networks [6]. This is expected to enable applications such as monitoring of areas with campus networks in intralogistics scenarios with humans and automatic guided vehicles (AGVs) as well as environment sensing for critical infrastructure or safe urban mobility [7], [8].

In monostatic ISAC setups where transmit and receiver are co-located, requirements related to full-duplex operation such as high isolation between transmit and receive antenna arrays and self-interference cancellation (SIC) are imposed [9], [10]. If, however, the transmitter and receiver are not co-located but rather widely separated, a bistatic ISAC setup is established [11]. In this case, the aforementioned full-duplex requirements are avoided, and existing deployments of cellular networks are exploited, achieving greater diversity of radar sensing measurements [12], [13]. In spite of its advantages, bistatic sensing comes at the cost of strict synchronization requirements to avoid biases in radar target parameter estimates such as bistatic range and Doppler shifts. When this is not achievable on hardware-level, e.g., via optical fiber connection between sensing gNodeBs (gNBs), over-the-air (OTA) synchronization must be performed.

In the context of bistatic sensing with cellular networks, recent studies in the literature have investigated bistatic radar sensing with fifth generation (5G) networks. Examples include [11], [14], [15], which consider bistatic sensing with a gNB acting as an illuminator of opportunity and a receiver having two separate antennas and radio-frequency (RF)/baseband (BB) channels for the reference and sensing links. In a previous study [16], a orthogonal frequency-division multiplexing (OFDM)-based bistatic ISAC system concept was proposed. Unlike the passive case, this concept is based on actively beamforming the a single transmit signal from a transmitting gNB towards both the receiving gNB and the directions of radar targets. At the receiver side, beams are pointed in the direction of the transmitting gNB, creating a reference path for sensing, as well as in the illuminated directions by the transmitting gNB where potential targets are located. The aforementioned reference line-of-sight (LoS) between is used for synchronization and communication, allowing to estimate the full transmit OFDM frame and use it for radar signal processing [17] to generate a bistatic radar image.

It was observed in [16] that small inaccuracies can be tolerated for time and frequency synchronization without biasing

Manuscript received DD MM, 2024. The authors acknowledge the financial support by the Federal Ministry of Education and Research of Germany in the projects “KOMSENS-6G” (grant number: 16KISK123) and “Open6GHub” (grant number: 16KISK010). (*Corresponding author: Lucas Giroto de Oliveira.*)

L. Giroto de Oliveira, Y. Li, T. Zwick, and B. Nuss are with the Institute of Radio Frequency Engineering and Electronics (IHE), Karlsruhe Institute of Technology (KIT), 76131 Karlsruhe, Germany (e-mail: lucas.oliveira@kit.edu, yueheng.li@kit.edu, thomas.zwick@kit.edu, benjamin.nuss@kit.edu).

S. Mandelli and M. Henninger are with Nokia Bell Laboratories, 70469 Stuttgart, Germany (e-mail: silvio.mandelli@nokia-bell-labs.com, marcus.henninger@nokia.com).

D. Brunner was with the Institute of Radio Frequency Engineering and Electronics (IHE), Karlsruhe Institute of Technology (KIT), 76131 Karlsruhe, Germany. He is now with VEGA Grieshaber KG, 77761 Schiltach, Germany (e-mail: d.brunner@vega.com).

X. Wan and T. J. Cui are with Southeast University, Nanjing, Jiangsu 12579, China (e-mail: wan_xiang@seu.edu.cn, tjcui@seu.edu.cn).

the radar target parameter estimates, as it is known that the LoS path should appear at null relative bistatic range and Doppler shift in the radar image and slight offsets can be therefore recognized. The sampling frequency offset (SFO), however, must be accurately estimated to avoid range and Doppler shift migration. These effects, which were also observed in and [18], result in signal-to-noise ratio (SNR) and resolution loss. It was also shown in [16] that the accuracy yielded by the algorithm by Tsai et al. [19] was not enough for unbiased bistatic sensing, and the discrete-time domain shifting of the OFDM symbols as described in [20] was adopted to correct the residual SFO. While such a measure is important as the SFO effects accumulate with increasing OFDM symbol index, which is particularly critical in ISAC applications where long frames are needed to achieve fine Doppler shift resolution and high processing gain, the aforementioned residual correction only compensates range migration, being ineffective against the SFO-induced Doppler shift migration.

An alternative delay-based SFO estimation approach was proposed by Wu et al. in [21]. In this approach, a correlation between the amplitudes of consecutive channel impulse response (CIR) estimates obtained based on pilot subcarriers is performed to estimate the SFO-induced delay migration and, as a next step, the SFO itself. While it is claimed in [22] that this approach might achieve inaccurate estimates depending on the adopted OFDM signal parameters, the proposed method by Wu et al. benefits from a discrete Fourier transform (DFT) processing gain proportional to the number of pilot subcarriers used to estimate each CIR [16]. This enhances the effective SNR for SFO estimation when compared to the phase-based method by Tsai et al. [19] that operates on the subcarrier level in the discrete-frequency domain. In addition, the CIR correlation method was proven to be effective in practice in [23]. The latter study, however, did not explicitly mention SFO in spite of mentioning the use of a Farrow filter [24] to correct non-ideal sampling, and it only dealt with the resulting range migration caused by residual SFO, not compensating the SFO-induced Doppler shift migration.

In this context, this article investigates an accurate pilot-based SFO estimation to enable further correction. This enables avoiding SFO-induced impairments to bistatic sensing in OFDM-based ISAC systems, namely SNR degradation and migration of range and Doppler shift. Assuming that the reference path is much stronger than the reflections off radar targets, delay-based estimation based on the method by Wu et al. is performed and analyzed. This method consists of estimating the delay migration of the reference path along consecutive CIR estimates obtained with OFDM symbols containing pilots, and then calculating its slope and converting it into an SFO estimate. While it does not profit from the contribution of target reflections to the effective SNR for SFO estimation, which in the assumed scenario is rather limited, it allows skipping the CIR correlation processing and therefore reducing computational complexity. This method, however, is susceptible to impairments caused by SFO-induced inter-carrier interference (ICI) and intersymbol interference (ISI), especially the latter one. Consequently, bias in the obtained SFO estimates cannot be ruled out.

To simultaneously ensure higher effective SNR for SFO estimation than in the method by Tsai et al. and avoid bias due to SFO-induced ISI in the method by Wu et al., therefore enabling robust communication and bistatic sensing, this article introduces the tilt inference of time offset (TITO) method. TITO performs the same estimation of the delay migration slope across consecutive CIR estimates to obtain an SFO estimation as in [21], but with an adaptive choice of the number of pilot OFDM symbols used to obtain CIR estimates. This complies with the flexible and irregular structure of 5G frame structures, where pilots might be available or not depending on the resource management decisions taken. In addition, it allows avoiding ISI-contaminated delay migration estimation, which would ultimately bias the obtained SFO estimate.

In addition to the proposed TITO method for SFO estimation, this article also addresses the challenge of achieving a dominant path with constant range, Doppler shift, and angle in a non-line-of-sight (NLoS) scenario. This is particularly important, e.g., in indoor deployments or when at least one of the gNBs constituting the bistatic pair is at street level, as no LoS is available in such cases. To this end, a system concept is proposed in which a reference path is assumed to be created via a relay reflective intelligent surface (RIS) [25]–[27], which redirects the incoming signal from the transmitting to the receiving ISAC node.

The contributions of this article can be summarized as follows:

- A detailed analysis of the effects of SFO, showing that it results in amplitude modulation of OFDM subcarriers, besides delay and frequency shift migration that may lead to relevant ISI and ICI, respectively. Finally, an approximate Cramér–Rao lower bound (CRLB) of the SFO estimation is analytically derived.
- To enhance estimation accuracy in spite of SFO-induced impairments, the TITO method is proposed, which is by-design robust against ISI. TITO also potentially requires lower computational complexity than [21] in cases with high SFO, as an adaptive number of pilot OFDM symbols is used.
- A comprehensive numerical analysis to support the claims and contributions of this article, illustrating the effect of the aforementioned SFO-induced impairments on synchronization, communication and sensing performances.
- A novel system concept for bistatic ISAC scenarios is proposed and demonstrated in practice. It consists of a transmitter and a receiver, both performing RIS-assisted beamsteering, besides a relay RIS to establish a static reference path when transmitter and receiver are not in LoS. This path is used to enable synchronization and communication, besides serving as reference to estimate range and Doppler of radar targets.
- Measurement results with the RIS-based setup to demonstrate the superiority of the TITO method over alternative SFO estimation approaches from the literature.

The remainder of this article is organized as follows. Section II presents the proposed RIS-assisted bistatic ISAC

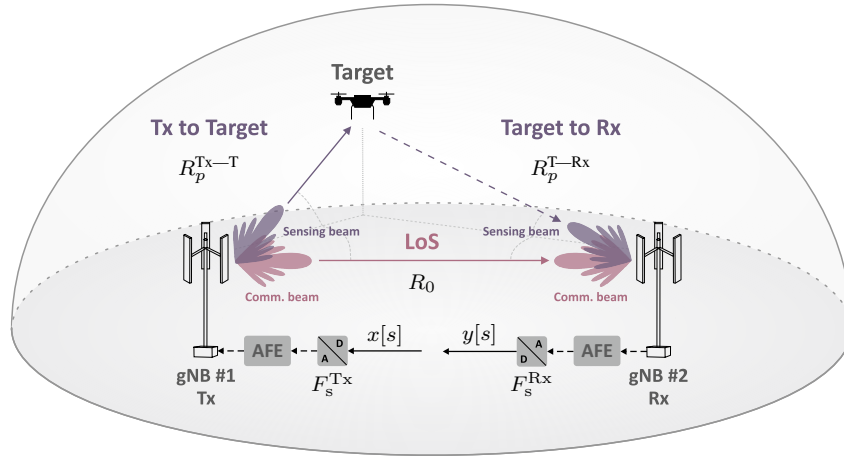


Fig. 1. Bistatic ISAC system representation.

system concept assuming OFDM as a modulation scheme. Next, Section III describes the effects of SFO on the receive OFDM signal and formulates both the delay migration-based SFO estimation approach derived from the method by Wu et al. [21] and the proposed TITO method, also deriving accuracy bounds and discussing SFO correction approaches. Section IV then presents a numerical analysis of the SFO effects on both communication and sensing performances, besides analyzing the SFO estimation performance of the TITO method. Finally, measurement results are presented in Section V, and concluding remarks are given in Section VI.

II. SYSTEM MODEL

In the considered bistatic ISAC system, which is depicted in Fig. 1, two gNodeBs (gNBs) are present. The first, gNB #1, acts as a transmitter, while the second, gNB #2, operates in the receiving mode. It is also assumed that there are P propagation paths between the gNBs labeled as $p \in \{0, 1, \dots, P-1\}$. The first, $p=0$, is a reference path created by the gNBs via beamforming, which enables synchronization and communication, besides providing a benchmark for bistatic radar sensing following the framework from [16]. This path has length R_0 that results in a propagation delay $\tau_0 = R_0/c_0$, where c_0 is the speed of light in vacuum, and Doppler shift $f_{D,0} = 0$ Hz since the gNBs are static. In Fig. 1, this reference is assumed to be a LoS path. Beams are also pointed from both gNB #1 and gNB #2 towards point targets that are associated with the remaining $P-1$ propagation paths. It is assumed that the p th path, $p \in \{1, \dots, P-1\}$, has length $R_p = R_p^{\text{Tx-T}} + R_p^{\text{T-Rx}}$, where $R_p^{\text{Tx-T}}$ and $R_p^{\text{T-Rx}}$ are the ranges of the associated point target with this path w.r.t. gNB #1 and gNB #2, respectively. Due to the propagation through this path, a delay $\tau_p = R_p/c_0$ is experienced. In addition, the movement of the point target associated with the p th path results in a Doppler

shift $f_{D,p} = (2v_p/\lambda_0) \cos(\gamma_p) \cos(\psi_p/2)$, where v_p is the magnitude of the tridimensional velocity vector, γ_p is the aspect angle referenced to the bistatic bisector, and ψ_p is the bistatic angle, all associated with the point target [28]. To ensure that targets are correctly illuminated, the beamforming directions at gNB #1 and gNB #2 can be previously estimated via hierarchical beam search [29] or other possibly more efficient strategies such as an extension of the sampling and reconstruction of the angular domain proposed in [30] to the bistatic case. Furthermore, power allocation among the dedicated beams to the reference path or to the sensing of targets can be performed aiming to meet communication and radar sensing performance requirements [31], [32].

At gNB #1, a discrete-frequency domain transmit frame $\mathbf{X} \in \mathbb{C}^{N \times M}$ with $M \in \mathbb{N}_{>0}$ OFDM symbols, each with $N \in \mathbb{N}_{>0}$ subcarriers, is generated. Each OFDM symbol undergoes inverse discrete Fourier transform (IDFT) and has cyclic prefix (CP) of length $N_{\text{CP}} \in \mathbb{N}_{\geq 0}$ prepended to it. The resulting discrete-time domain sequence $x[s] \in \mathbb{C}$, $s \in \{0, 1, \dots, M(N + N_{\text{CP}}) - 1\}$, from parallel-to-serial (P/S) conversion on \mathbf{X} then undergoes digital-to-analog (D/A) conversion with sampling rate F_s^{Tx} , whose corresponding sampling period is $T_s^{\text{Tx}} = 1/F_s^{\text{Tx}}$. This results in a baseband transmit signal $x(t) \in \mathbb{C}$ that occupies a bandwidth $B \leq F_s^{\text{Tx}}$. Consequently, the subcarrier spacing in the frequency domain is $\Delta f = B/N$. After conditioning by the analog front-end (AFE), transmission at the carrier frequency $f_c \gg B$, and reception at gNB #2, the baseband receive signal $y(t) \in \mathbb{C}$ at the receiving ISAC node in the considered system is expressed as in (1). In this equation, the attenuation factor α_0 , which accounts for all losses in the reference path from gNB #1 to gNB #2, is given by

$$\alpha_0 = \sqrt{\frac{G_{\text{Tx}} G_{\text{Rx}} \lambda_0^2}{(4\pi)^3 R_0^4}}, \quad (2)$$

$$y(t) = \alpha_0 x(t - \tau_0 - \tau_{\Delta}) e^{j2\pi f_{\Delta} t + \psi_{\Delta}} + \sum_{p=1}^{P-1} \alpha_p x(t - \tau_p - \tau_{\Delta}) e^{j2\pi f_{D,p} t} e^{j2\pi f_{\Delta} t + \psi_{\Delta}} \quad (1)$$

where G_{Tx} and G_{Rx} are the combined single-antenna and beamforming gains at gNBs #1 and #2, respectively. In addition, $\lambda_0 = c_0/f_c$ is the wavelength associated with the carrier frequency f_c . The attenuation factor α_p for the p th propagation path associated with a point target can be expressed as

$$\alpha_p = \sqrt{\frac{G_{\text{Tx}}G_{\text{Rx}}\sigma_{\text{RCS},p}\lambda_0^2}{(4\pi)^3 R_p^{\text{T-Rx}^2} R_p^{\text{R-T}^2}}}. \quad (3)$$

In this equation, $\sigma_{\text{RCS},p}$ denotes the bistatic radar cross section (RCS) of the point target associated with the p th path, which is aspect-dependent. In other words, $\sigma_{\text{RCS},p}$ depends on the angle from which the target is illuminated by gNB #1 and the angle to which reflections are directed towards gNB #2. Regarding τ_Δ , f_Δ , and ψ_Δ , they respectively represent the symbol time offset (STO) τ_Δ caused by the mismatch between transmitter and receiver time references, the carrier frequency offset (CFO) f_Δ and its resulting phase rotation ψ_Δ between the oscillators at transmitter and receiver ISAC nodes.

Next, it is assumed that the baseband signal $y(t)$ is sampled with the sampling frequency F_s^{Rx} at the receiver at the time instants sT_s^{Rx} , where $T_s^{\text{Rx}} = 1/F_s^{\text{Rx}}$ is the sampling period at the receiver. The aforementioned sampling produces the sequence $y[s] \in \mathbb{C}$. For the sake of simplicity, it is assumed that the adopted sampling rate F_s^{Rx} at the receiver of the bistatic ISAC system is exactly the same as F_s^{Tx} adopted at the transmitter side, which results in the non-occurrence of SFO. It is further assumed that the length N_{CP} of the CP prepended to the OFDM symbols at the transmitter side is sufficient to avoid ISI due to propagation, and that STO and CFO are estimated and corrected. The aforementioned synchronization can be performed, e.g., using the reference path and relying on fully known preamble OFDM symbols [33] or, as in the 5G new radio (NR) case, partly known preamble OFDM symbols [34]. Consequently, a receive OFDM frame $\tilde{\mathbf{Y}} \in \mathbb{C}^{N \times M}$ can be formed by removing CP and performing a DFT on each OFDM symbol extracted from the resulting samples after performing time and frequency synchronization on $y[s]$. The element $\tilde{Y}_{n,m} \in \mathbb{C}$ at the n th row, $n \in \{-N/2, 1, \dots, N/2 - 1\}$, and m th column, $m \in \{0, 1, \dots, M - 1\}$, of $\tilde{\mathbf{Y}}$ can be expressed as in (4) [16]. In this equation, $X_{n,m} \in \mathbb{C}$ is the element at the n th row and m th column of the transmit OFDM frame in the discrete-frequency domain \mathbf{X} . In practice, however, SFO occurs, which leads to different F_s^{Rx} and F_s^{Tx} and, consequently, to degradation of the receive OFDM frame $\tilde{\mathbf{Y}}$. Consequently, the SFO must be estimated and corrected before communication processing to estimate the transmit

frame \mathbf{X} and subsequent bistatic radar sensing processing as described in [16] can be performed.

III. PILOT-BASED SFO ESTIMATION AND CORRECTION

If the adopted sampling rate F_s^{Rx} to perform analog-to-digital conversion on $y(t)$ to produce $y[s]$ at the receiver side is different than F_s^{Tx} , then SFO occurs. The experienced SFO is given by

$$\text{SFO} = F_s^{\text{Rx}} - F_s^{\text{Tx}}, \quad (5)$$

and normalized SFO by the transmit sampling rate F_s^{Tx} is defined as $\delta \in \mathbb{R}$ and expressed as

$$\delta = \frac{\text{SFO}}{F_s^{\text{Tx}}} = \frac{F_s^{\text{Rx}} - F_s^{\text{Tx}}}{F_s^{\text{Tx}}}. \quad (6)$$

For a non-zero normalized SFO δ , $y[s]$ becomes

$$y[s] = y(t) \Big|_{t=sT_s^{\text{Tx}}(1-\delta)} + w[s], \quad (7)$$

where $w[s] \in \mathbb{C}$ is the sampled additive white Gaussian noise (AWGN). Consequently, the receive OFDM frame $\tilde{\mathbf{Y}}$ still assuming fully corrected STO and CFO becomes $\mathbf{Y} \in \mathbb{C}^{N \times M}$. For small SFOs that do lead to ISI, the element $Y_{n,m} \in \mathbb{C}$ at the n th row and m th column of \mathbf{Y} can be expressed as [35], [36]

$$Y_{n,m} = \alpha_n^{\text{SFO}} \left(\tilde{Y}_{n,m} \right) e^{j\psi_{n,m}^{\text{SFO}}} + \xi_{n,m}^{\text{SFO,ICI}} + W_{n,m}, \quad (8)$$

where $\alpha_n^{\text{SFO}} \in \mathbb{R}_{\geq 0}$ is an amplitude modulation expressed as

$$\alpha_n^{\text{SFO}} = \frac{\sin(\pi\delta n)}{N \sin\left(\frac{\pi\delta n}{N}\right)}, \quad (9)$$

$\psi_{n,m}^{\text{SFO}} \in \mathbb{R}$ is a phase rotation expressed as

$$\psi_{n,m}^{\text{SFO}} = -\frac{2\pi\delta n}{N} [m(N + N_{\text{CP}}) + N_{\text{CP}}] - \frac{\pi\delta n}{N} (N - 1), \quad (10)$$

and $\xi_{n,m}^{\text{SFO,ICI}} \in \mathbb{C}$ is the ICI term expressed as in (11), and $W_{n,m} \in \mathbb{C}$ is the equivalent sampled AWGN at the n th subcarrier of the m th OFDM symbol in the frame.

Rearranging the first term of (10) and resorting to the DFT shift theorem, it is concluded that the SFO causes a delay that is equal to

$$\tau_m^{\text{SFO}} = \delta [m(N + N_{\text{CP}}) + N_{\text{CP}}] T_s \quad (12)$$

at the m th OFDM symbol. Since τ_m^{SFO} changes with m , a delay migration defined as

$$\Delta\tau_m^{\text{SFO}} = \tau_m^{\text{SFO}} - \tau_0^{\text{SFO}} = \delta [m(N + N_{\text{CP}})] T_s \quad (13)$$

$$\tilde{Y}_{n,m} \approx \alpha_0 X_{n,m} e^{j\psi_\Delta} + \sum_{p=1}^{P-1} \alpha_p X_{n,m} e^{-j2\pi n \Delta f (\tau_p - \tau_0)} e^{j2\pi f_{D,p} [m(N + N_{\text{CP}}) + N_{\text{CP}}] / B} e^{j\psi_\Delta} \quad (4)$$

$$\xi_{n,m}^{\text{SFO,ICI}} = \sum_{l=-N/2, l \neq n}^{N/2-1} \tilde{Y}_{l,m} \frac{\sin(\pi[(1+\delta)l-n])}{N \sin\left(\frac{\pi[(1+\delta)l-n]}{N}\right)} e^{j2\pi \frac{m(N + N_{\text{CP}}) + N_{\text{CP}}}{N} \delta l} e^{j\pi \frac{N-1}{N} [(1+\delta)l-n]} \quad (11)$$

is experienced along the OFDM symbols in \mathbf{Y} . Comparing (8) with the effect of a CFO on the receive OFDM symbol as described in [35], it is also concluded that the normalized SFO δ causes a frequency shift equal to

$$f_n^{\text{SFO}} = (\delta n)\Delta f \quad (14)$$

at the n th subcarrier of every OFDM symbol, which corresponds to the n th row of \mathbf{Y} . As f_n^{SFO} is a function of n , a frequency shift migration

$$\Delta f^{\text{SFO}} = f_{N/2-1}^{\text{SFO}} - f_{-N/2}^{\text{SFO}} \quad (15)$$

is experienced from the first to the last OFDM subcarrier in each OFDM symbol contained in \mathbf{Y} .

By estimating the previously described SFO-induced impairments to the reference path, the SFO itself can be estimated. For that purpose, either preamble OFDM symbols [16], [37] or pilot subcarriers can be used under the condition that they are known at the receiver side. The first approach, however, leads to undesirable overhead, reducing the communication data rate. By using only pilot subcarriers, a possible approach to estimate the SFO is by observing the frequency shift migration along consecutive pilot subcarriers along the OFDM symbols. To improve the effective SNR for SFO estimation, the delay migration can be observed instead. This approach consists of obtained channel frequency response (CFR) estimates from the pilot subcarriers in \mathbf{Y} [38], [39], and transforming them into CIR estimates via IDFTs. From these CIR estimates, the delay migration, and consequently, the SFO can be estimated. This approach benefits from a processing gain that is to the one experienced during range processing in OFDM-based radar and ISAC systems [17]. Consequently, higher effective SNR and better accuracy for SFO estimation is experienced than in the approach based on frequency shift migration that operates on the subcarrier level.

An SFO estimation approach based on delay migration has been proposed by Wu et al. [21], which however has not provided accuracy bounds to their estimator. In this sense, Section III-A describes an SFO estimation approach based on [21], highlighting its limitations and providing accuracy bounds. To ensure higher robustness at SFO-induced ISI and reduce computational complexity at higher SFOs, the TITO method is presented in Section III-B. Finally, Section III-C discusses SFO correction strategies that can be performed once it has been estimated.

A. Delay migration-based SFO estimation

Assuming sufficient SNR regime, negligible SFO-induced ICI and no SFO-induced ISI at every m th OFDM symbol, one can use the pilot subcarriers in \mathbf{Y} to obtain CIR estimates. In this article, they are assumed to be uniformly distributed for simplicity, as depicted in Fig. 2. In practical implementations such as 5G NR, demodulation reference signal (DMRS) [40] could be used as the aforementioned pilot subcarriers at first assessment, as it is present in sufficient density in the OFDM frame and does not introduce communication overhead. However, the beamforming coefficients associated with DMRS defined at gNB #1 are different across the

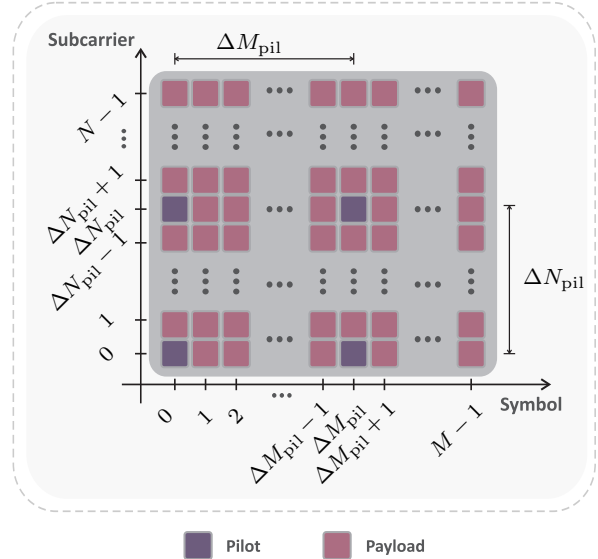


Fig. 2. Structure of the OFDM frame \mathbf{X} in the discrete-frequency domain.

subcarriers and not known at the receiver in gNB #2 due to user equipment (UE)-specific precoding. Consequently, this may prevent using DMRS to obtain the required CIR estimates for SFO estimation. An alternative solution is to reposition reference signal (PRS) [41], [42] subcarriers for SFO estimation, as it adopts known, constant beamforming coefficients.

The obtained CIR estimates from the pilot subcarriers in \mathbf{Y} form a delay-slow time profile represented by the matrix $\mathbf{D} \in \mathbb{C}^{N_{\text{pil}} \times M_{\text{pil}}}$. To ensure fine delay granularity in the contained CIR estimates in \mathbf{D} and therefore improve the accuracy of estimated delays, the required IDFT processing can be zero padded. The m_{pil} th column, $m_{\text{pil}} \in \{0, 1, \dots, M_{\text{pil}} - 1\}$, of the \mathbf{D} contains one CIR estimate obtained from the N_{pil} pilot subcarriers at the corresponding pilot OFDM symbol. Assuming spacing ΔN_{pil} and ΔM_{pil} between pilot subcarriers in the column and row directions in the OFDM frame, it holds that

$$N_{\text{pil}} = \left\lfloor \frac{N}{\Delta N_{\text{pil}}} \right\rfloor + 1, \quad (16)$$

and

$$M_{\text{pil}} = \left\lfloor \frac{M}{\Delta M_{\text{pil}}} \right\rfloor + 1. \quad (17)$$

Since the assumed uniform pilot subcarrier spacing may not be observed in practical deployments, it is also worth highlighting that it is not required for delay migration and consequent SFO estimation.

To estimate the residual SFO, the proposed method, TITO, is applied to the reference path enabled by the relay RIS. In this context, the aforementioned path is taken as a benchmark and its delay progression along the successive CIR estimates contained in the columns of \mathbf{D} is analyzed. For that purpose, the delay migration of the aforementioned path is estimated at every m_{pil} th column of \mathbf{D} , yielding $\widehat{\Delta\tau}_{\text{pil}, m_{\text{pil}}}^{\text{SFO}}$. Knowing that the correspondence between column indexes from \mathbf{D} and \mathbf{Y} is given by

$$m = m_{\text{pil}}\Delta M_{\text{pil}}, \quad (18)$$

it holds that

$$\widehat{\Delta\tau}_{\text{pil},m_{\text{pil}}}^{\text{SFO}} = \widehat{\Delta\tau}_{m_{\text{pil}}\Delta M_{\text{pil}}}^{\text{SFO}}. \quad (19)$$

In this equation, $\widehat{\Delta\tau}_{m_{\text{pil}}\Delta M_{\text{pil}}}^{\text{SFO}}$ denotes an estimate of $\Delta\tau_{m_{\text{pil}}\Delta M_{\text{pil}}}^{\text{SFO}}$. By feeding all M_{pil} delay migration estimates $\widehat{\Delta\tau}_{\text{pil},m_{\text{pil}}}^{\text{SFO}}$ to a linear regression model based on (13), a least squares (LS) estimate $\widehat{\delta}$ of the normalized SFO is finally obtained. This is achieved by taking the partial derivative of the sum of the squared differences to be minimized in (20) w.r.t. δ , setting it to zero and solving to yield $\widehat{\delta}$, which is expressed as in (21).

Due to the linear regression nature of the SFO estimation, the estimate $\widehat{\delta}$ has a standard deviation $\sigma_{\widehat{\delta}}$ given by (22). This equation shows that $\sigma_{\widehat{\delta}}$ depends on the standard deviation $\sigma_{\widehat{\Delta\tau}_{\text{pil},m_{\text{pil}}}^{\text{SFO}}}$ of the delay migration estimates at each m_{pil} th column of \mathbf{D} . Based on the CRLB of delay migration estimation in OFDM-based systems at high SNR [43], the lower bound for $\sigma_{\widehat{\Delta\tau}_{\text{pil},m_{\text{pil}}}^{\text{SFO}}}$ assuming negligible SFO-induced ICI and ISI is

$$\sigma_{\widehat{\Delta\tau}_{\text{pil},m_{\text{pil}}}^{\text{SFO}}} \geq \sqrt{\frac{6}{\text{SNR}(N_{\text{pil}}^2 - 1)N_{\text{pil}}} \left(\frac{1}{2\pi\Delta f\Delta N_{\text{pil}}} \right)^2}. \quad (23)$$

The SNR in this equation is calculated assuming that the receive signal in the considered RIS-assisted bistatic ISAC system is impaired by AWGN, being therefore given by

$$\text{SNR} = \frac{P_{\text{Tx}}\alpha_c^2\beta_c^2}{k_{\text{B}} B T_{\text{therm}} \text{NF}}, \quad (24)$$

where k_{B} is the Boltzmann constant, T_{therm} is the standard room temperature in Kelvin, and NF is the overall receiver noise figure. Based on (22) and (23), a lower bound for $\sigma_{\widehat{\delta}}$ at high SNR and still assuming negligible SFO-induced ICI and ISI can be defined as in (25). While this lower bound can only be reached by unbiased estimators such as multiple signal classification (MUSIC). In practical deployments, however, if the processing based on zero-padded IDFTs is used as a maximum likelihood estimator (MLE), then bias occurs due to the limited granularity of the axis of possible delays that can be estimated: This axis is solely composed by integer multiples of $1/(\eta B)$, where $\eta \in \mathbb{N}_{\geq 1}$ is the zero padding (ZP) factor. Consequently, a more accurate lower bound for $\sigma_{\widehat{\Delta\tau}_{\text{pil},m_{\text{pil}}}^{\text{SFO}}}$ at high SNR is given by [43]

$$\sigma_{\widehat{\Delta\tau}_{\text{pil},m_{\text{pil}}}^{\text{SFO}}} \geq \frac{\sqrt{3}}{6\eta N_{\text{pil}}\Delta f\Delta N_{\text{pil}}}. \quad (26)$$

Consequently, a lower bound for $\sigma_{\widehat{\delta}}$ for the case in which $\widehat{\delta}$ is obtained based on MLE delay migration estimates $\widehat{\Delta\tau}_{\text{pil},m_{\text{pil}}}^{\text{SFO}}$ can be defined as in (27). Since the MLE error is actually uniformly distributed due to the quantized zero-padded IDFT bins, the aforementioned lower bound is only a simplified approximation.

In order for the SFO estimation to work as intended, i.e., without relevant performance degradation or bias, the experienced normalized SFO δ should not induce ICI and ISI that result in relevant degradation of the reference path in the CIRs estimates in the columns of \mathbf{D} . Some remarks on these issues are presented as follows.

$$\widehat{\delta} = \arg \min_{\delta} \sum_{m_{\text{pil}}=0}^{M_{\text{pil}}-1} \left(\widehat{\Delta\tau}_{\text{pil},m_{\text{pil}}}^{\text{SFO}} - \{\delta [(m_{\text{pil}}\Delta M_{\text{pil}})(N + N_{\text{CP}})] T_{\text{s}} \} \right)^2 \quad (20)$$

$$\widehat{\delta} = \frac{M_{\text{pil}} \sum_{m_{\text{pil}}=0}^{M_{\text{pil}}-1} [(m_{\text{pil}}\Delta M_{\text{pil}})(N + N_{\text{CP}})T_{\text{s}}] \widehat{\Delta\tau}_{\text{pil},m_{\text{pil}}}^{\text{SFO}} - \sum_{m_{\text{pil}}=0}^{M_{\text{pil}}-1} [(m_{\text{pil}}\Delta M_{\text{pil}})(N + N_{\text{CP}})T_{\text{s}}] \sum_{m_{\text{pil}}=0}^{M_{\text{pil}}-1} \widehat{\Delta\tau}_{\text{pil},m_{\text{pil}}}^{\text{SFO}}}{M_{\text{pil}} \sum_{m_{\text{pil}}=0}^n [(m_{\text{pil}}\Delta M_{\text{pil}})(N + N_{\text{CP}})T_{\text{s}}]^2 - \left[\sum_{m_{\text{pil}}=0}^{M_{\text{pil}}-1} (m_{\text{pil}}\Delta M_{\text{pil}})(N + N_{\text{CP}})T_{\text{s}} \right]^2} \quad (21)$$

$$\sigma_{\widehat{\delta}} \approx \frac{\sigma_{\widehat{\Delta\tau}_{\text{pil},m_{\text{pil}}}^{\text{SFO}}}}{\sqrt{M_{\text{pil}} \sum_{m_{\text{pil}}=0}^n [(m_{\text{pil}}\Delta M_{\text{pil}})(N + N_{\text{CP}})T_{\text{s}}]^2 - \left[\sum_{m_{\text{pil}}=0}^{M_{\text{pil}}-1} (m_{\text{pil}}\Delta M_{\text{pil}})(N + N_{\text{CP}})T_{\text{s}} \right]^2}} \quad (22)$$

$$\sigma_{\widehat{\delta}} \gtrsim \sqrt{\frac{\{6/[\text{SNR}(N^2 - 1)N]\} [1/(2\pi\Delta f\Delta N_{\text{pil}})]^2}{M_{\text{pil}} \sum_{m_{\text{pil}}=0}^n [(m_{\text{pil}}\Delta M_{\text{pil}})(N + N_{\text{CP}})T_{\text{s}}]^2 - \left[\sum_{m_{\text{pil}}=0}^{M_{\text{pil}}-1} (m_{\text{pil}}\Delta M_{\text{pil}})(N + N_{\text{CP}})T_{\text{s}} \right]^2}} \quad (25)$$

$$\sigma_{\widehat{\delta}} \gtrsim \frac{\sqrt{3}/(6\eta N_{\text{pil}}\Delta f\Delta N_{\text{pil}})}{\sqrt{M_{\text{pil}} \sum_{m_{\text{pil}}=0}^n [(m_{\text{pil}}\Delta M_{\text{pil}})(N + N_{\text{CP}})T_{\text{s}}]^2 - \left[\sum_{m_{\text{pil}}=0}^{M_{\text{pil}}-1} (m_{\text{pil}}\Delta M_{\text{pil}})(N + N_{\text{CP}})T_{\text{s}} \right]^2}} \quad (27)$$

Remark 1. It is ideally expected that normalized SFO δ only results in frequency shifts f_n^{SFO} that cause negligible ICI.

Elaboration. To avoid non-negligible ICI that will eventually lead to degradation of the delay and consequently SFO estimation and its subsequent correction, the SFO-induced frequency shift f_n^{SFO} at every n th OFDM subcarriers must be significantly lower than the subcarrier spacing Δf . Assuming the typical frequency shift upperbound for OFDM systems of one tenth of Δf [17], [44],

$$f_n^{\text{SFO}} < \Delta f/10 \quad (28)$$

should hold to result in negligible ICI. Combining (28) with (14) results in $(\delta n)\Delta f < \Delta f/10$. Applying (28) to the highest absolute SFO-induced ICI, which is experienced at $n = \pm N/2$, results in

$$|\delta| < \delta_{\max}^{\text{ICI}}, \quad (29)$$

where

$$\delta_{\max}^{\text{ICI}} = 1/(5N). \quad (30)$$

Note that, while subcarrier $n = -N/2$ exists, $n = N/2$ is only approached when performing zero-padding. ■

Remark 2. It is ideally expected that the normalized SFO δ only results in delays τ_m^{SFO} that do not cause ISI.

Elaboration. To avoid ISI-induced performance degradation of the delay and SFO estimation and therefore of the RIS-assisted bistatic ISAC system as a whole, ISI should not happen at any of the OFDM symbols in the frame. If the SFO-induced delay τ_m^{SFO} is negative, ISI will necessarily occur. For positive delays, however, τ_m^{SFO} at all OFDM symbols, regardless of whether they contain pilots or not, should be lower than the CP-free delay $\tau_{\max}^{\text{CP}} = N_{\text{CP}}/B$. Therefore, it should hold that

$$\tau_{\max}^{\text{CP}} > \tau_{m_{\text{pil}}}^{\text{SFO}} \geq 0. \quad (31)$$

Consequently, the delay τ_{M-1}^{SFO} at the $(M-1)$ th column of \mathbf{Y} should be such that

$$N_{\text{CP}}/B > \tau_{M-1}^{\text{SFO}} \geq 0. \quad (32)$$

Based on (12), this results in

$$\delta_{\max}^{\text{ISI}} > \delta \geq 0, \quad (33)$$

where

$$\delta_{\max}^{\text{ISI}} = \frac{N_{\text{CP}}}{B[(M-1)(N+N_{\text{CP}}) + N_{\text{CP}}]T_s}. \quad (34)$$

B. TITO method for ISI-aware SFO estimation

As discussed in Section III-A, the presented approximate lower bounds for the SFO estimates in (25) and (27) so far are only accurate under the assumption of negligible SFO-induced ICI and ISI. The aforementioned ICI is expected to be handled by the previously mentioned processing gain of $10 \log_{10}(N_{\text{pil}})$ dB at the delay migration estimation. The SFO-induced ISI, however, can severely degrade the

delay migration estimation [45] and, consequently, the SFO estimation. In order to avoid this, the TITO method for SFO estimation is proposed. This method consists of performing the described SFO estimation based on the slope (or tilt) estimation (or inference) of the delay (or time offset) migration of the reference path along CIR estimates contained in the columns of \mathbf{D} in Section III-A, which ultimately allows obtaining an estimate $\hat{\delta}$ of the normalized SFO based on the knowledge of its relationship with the delay migration described by (13). The novelty of TITO compared to approaches such as the one based on the method by Wu et al. [21] lies in the adaptive choice of the number $M_{\text{pil}}^{\text{TITO}} \leq M_{\text{pil}}$ of columns of \mathbf{D} to be used for delay migration and subsequent SFO estimation with the aim of avoiding using CIR estimates that originate from ISI-contaminated pilot OFDM symbols, which is explained as follows. First, it is important to highlight that ISI only happens at the pilot OFDM symbols of index m_{pil} where the SFO-induced delay $\tau_{m_{\text{pil}}}^{\text{SFO}}$ is either negative or positive and exceeds the CP duration $N_{\text{CP}}T_s^{\text{Tx}}$. In both cases, the ISI-induced signal-to-interference-plus-noise ratio (SINR) degradation of the reference path in the aforementioned CIR estimates depends on the SFO-induced excess delay causing the ISI. Considering these issues, only the $M_{\text{pil}}^{\text{TITO}}$ first columns of \mathbf{D} where tolerable SINR degradation is experienced are used to obtain the required delay migration estimates for the SFO estimation with the TITO method. This also results in lower computational complexity compared with the method by Wu et al. [21] in cases with high SFO, since only a limited number of columns of \mathbf{D} are used for CIR and subsequent SFO estimation. Based on (13), $M_{\text{pil}}^{\text{TITO}}$ is chosen such that

$$\begin{aligned} M_{\text{pil}}^{\text{TITO}} &= \max m_{\text{pil}} + 1 \\ \text{s.t.} \quad &\left| \frac{\widehat{\Delta\tau}_{\text{pil}, m_{\text{pil}}}^{\text{SFO}} - \widehat{\Delta\tau}_{\text{pil}, m_{\text{pil}}-1}^{\text{SFO}}}{\Delta M_{\text{pil}}(N + N_{\text{CP}})T_s^{\text{Tx}}} \right| \leq (1 + \varepsilon)|\delta_{\max}|. \end{aligned} \quad (35)$$

In (35), $|\delta_{\max}| \in \mathbb{R}_{\geq 0}$ is the maximum absolute normalized SFO (positive or negative) that is expected in the RIS-assisted bistatic ISAC system. Furthermore, ε denotes an empirically defined margin that accounts for factors that influence the delay migration estimation inaccuracies, such as the chosen ZP factor η in the MLE estimation and the SNR. If the constraint in (35) is violated, it is considered that the SFO-induced ISI causes significant SINR degradation that in turn leads to non-negligible bias in the delay migration estimates at pilot OFDM symbols of index $m_{\text{pil}} = M_{\text{pil}}^{\text{TITO}}$ or higher. The CIRs contained in \mathbf{D} which correspond to these pilot OFDM symbols are therefore discarded and only the $M_{\text{pil}}^{\text{TITO}}$ first columns of \mathbf{D} are considered for the delay migration estimation and subsequent SFO estimation. While this degrades the accuracy of the SFO estimation according to (25) and (27), it avoids biasing the SFO estimate $\hat{\delta}$ due to ISI as later shown in the results in Section IV. Finally, it is worth highlighting that, forcing $M_{\text{pil}}^{\text{TITO}} = M_{\text{pil}}$, the TITO SFO estimation method becomes equivalent to approach based on the method by Wu et al. [21].

TABLE I
ADOPTED OFDM SIGNAL PARAMETERS

Carrier frequency (f_c)	26.2 GHz
Frequency bandwidth (B)	500 MHz
No. of subcarriers (N)	2048
Subcarrier spacing (Δf)	244.14 kHz
CP length (N_{CP})	512
No. of OFDM symbols (M)	4096
Pilot spacing (ΔN_{pil} , ΔM_{pil})	2, 4
No. of pilot subc. per pilot OFDM symbol (N_{pil})	1024
No. of OFDM symbols w/ pilots (M_{pil})	1024
Digital modulation	QPSK
Channel coding and code rate	LDPC, 2/3

C. SFO correction

Once the estimate $\hat{\delta}$ has been obtained with (21) using a limited number of pilot OFDM symbols defined according to (35), resampling is performed on the discrete-time domain samples associated with the receive frame including CP. Typically, a Farrow filter [24] with previous cubic interpolation [46] is employed. After resampling, CP is removed and the OFDM symbols are once again transformed into the discrete-frequency domain for further communication processing to estimate the transmit frame \mathbf{X} and subsequent bistatic radar sensing processing as described in [16].

While the resampling approach is able to correct both low and high SFOs, a simplified correction can be performed for the case where the SFO is so low that negligible ICI and ISI occur. In this case, a zero forcing (ZF) equalization of $Y_{n,m}$ is performed to yield an estimate of $\tilde{Y}_{n,m}$. This estimate is given by $\hat{Y}_{n,m} = Y_{n,m} / (\hat{\alpha}_n^{\text{SFO}} e^{j\hat{\psi}_{n,m}^{\text{SFO}}})$, where $\hat{\alpha}_n^{\text{SFO}}$ and $\hat{\psi}_{n,m}^{\text{SFO}}$ are estimates of α_n^{SFO} and $\psi_{n,m}^{\text{SFO}}$ calculated by using $\hat{\delta}$ instead of its true value δ in (9) and (10), respectively. Since this method is assumed to be used for very low SFO only, $\alpha_n^{\text{SFO}} \approx 1$ is expected for all n , and the described equalization can be simplified to $\hat{Y}_{n,m} = Y_{n,m} / e^{j\hat{\psi}_{n,m}^{\text{SFO}}}$ or, alternatively,

$$\hat{Y}_{n,m} \approx \tilde{Y}_{n,m} + W_{n,m} / e^{j\hat{\psi}_{n,m}^{\text{SFO}}}. \quad (36)$$

The N rows and M columns filled with elements $\hat{Y}_{n,m}$ form a receive frame $\hat{\mathbf{Y}} \in \mathbb{C}^{N \times M}$, which can finally be used for the previously mentioned further processing. Since this approach only requires dividing each subcarrier in the discrete-frequency domain by a phase term, it results in lower computational complexity than imposed by resampling approach. This happens since the latter requires resampling the whole sequence $y[s]$, including samples belonging to the CPs of the OFDM symbols. In addition, DFT must be performed again for each OFDM symbol after serial-to-parallel conversion and CP removal to reconstruct the OFDM frame with corrected SFO.

IV. NUMERICAL RESULTS

In this section, the performance of the RIS-assisted bistatic ISAC system with the introduced TITO SFO estimation

TABLE II
COMMUNICATION AND RADAR PERFORMANCE PARAMETERS

Comm. data rate (100% duty cycle, $\mathcal{R}_{\text{comm}}$)	0.40 Gbit/s
Processing gain (G_p)	69.24 dB
Range resolution (ΔR)	0.60 m
Max. unamb. range ($R_{\text{max,ua}}$)	1227.95 m
Max. ISI-free range ($R_{\text{max,ISI}}$)	306.99 m
Doppler shift resolution (Δf_D)	47.68 Hz
Max. unamb. Doppler shift ($f_{D,\text{max,ua}}$)	97.66 kHz
Max. ICI-free Doppler shift ($f_{D,\text{max,ICI}}$)	24.41 kHz

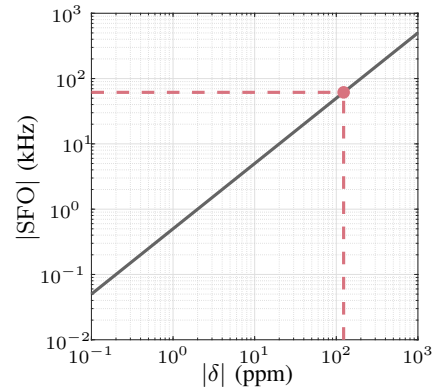


Fig. 3. Equivalent SFO in kHz to the normalized SFO to the Nyquist sampling rate $F_s = B$ (—). For reference, the maximum expected absolute value of the SFO in the bistatic setup from Section V based on two Zynq UltraScale+ RFSoc ZCU111 system-on-a-chip (SoC) platforms is also shown (●).

method is analyzed. For this purpose, the OFDM signal parameters listed in Table I, which according to [16], [17] result in the radar and communication performance parameters listed in Table II, are adopted. While these parameters do not comply, e.g., with 5G NR numerology, they were chosen to meet constraints of the measurement setup described later in Section V, allowing to achieve suitable communication and radar sensing performances.

A. SFO-induced impairment of ISAC system performance

Based on the adopted parameters, the corresponding SFO in kHz to δ , which represents the normalized SFO to the Nyquist sampling rate $F_s = B$, is shown in Fig. 3. In this figure, the maximum normalized SFO of ± 123 ppm expected with the adopted measurement setup later described in Section V based on two distinct Zynq UltraScale+ RFSoc ZCU111 SoC platforms is also shown. This number derives from the stability of ± 61.5 ppm of the programmable clocks at each board, from which the sampling clocks are derived, and it represents a common normalized SFO expected in practice.

Next, the SFO-induced impairments to the discrete-frequency domain OFDM frame \mathbf{Y} apart from ISI discussed in Section III, namely the amplitude modulation α_n^{SFO} , the delay migration $\Delta\tau_m^{\text{SFO}}$, and the subcarrier frequency shift f_n^{SFO} , are shown in Fig 4 for $|\delta| \in \{0, 0.1, 1, 10, 100, 1000\}$ ppm. It can be seen in Fig. 4(a) that all considered SFO values except for $|\delta| = 1000$ ppm yield negligible amplitude modulation along the subcarrier index n . In Figs. 4(b) and (c),

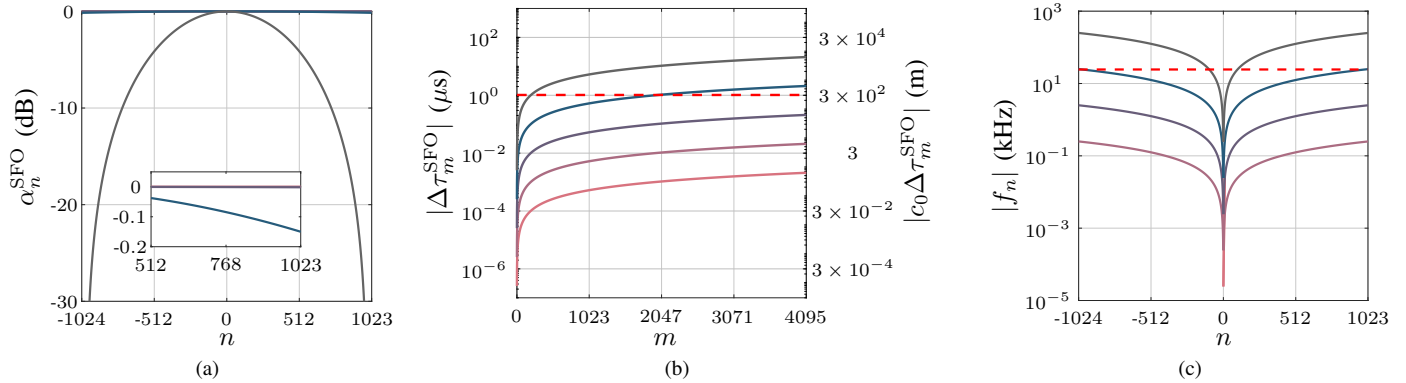


Fig. 4. SFO effects: (a) amplitude modulation α_n^{SFO} along the subcarriers, (b) absolute value of the delay migration $\Delta\tau_m^{\text{SFO}}$ along the OFDM symbols, and (c) absolute value of the subcarrier frequency shift f_n^{SFO} along the subcarriers, all evaluated for $|\delta| = 0.1$ ppm (—), $|\delta| = 1$ ppm (—), $|\delta| = 10$ ppm (—), $|\delta| = 100$ ppm (—), and $|\delta| = 1000$ ppm (—). For comparison with the achieved values, the maximum ISI-free delay of N_{CP}/B and range of $c_0 N_{\text{CP}}/B$ for the positive δ case, as well as the maximum tolerable frequency shift of $\Delta f/10$ defined in (28) which causes negligible ICI are marked (—) in (b) and (c), respectively.

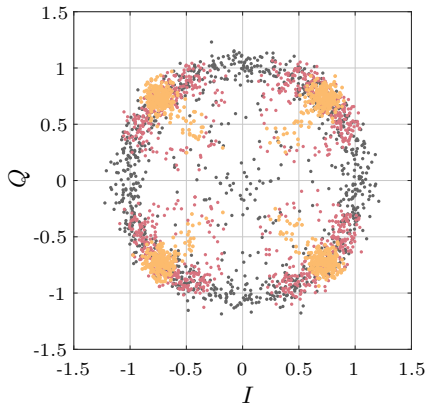


Fig. 5. Normalized receive quadrature phase-shift keying (QPSK) constellations obtained from simulations for an AWGN channel with SNR = 20 dB and $\delta = 1$ ppm at OFDM symbols $m = 0$ (●), EVM = -21.39 dB, $m = 64$ (●, EVM = -13.05 dB), and $m = 4094$ (●, EVM = 0.18 dB).

however, it is seen that $|\delta| \in \{100, 1000\}$ ppm yield delays and frequency shifts that exceed both the ICI- and ISI-free SFO limits defined according to (29) and (33), respectively. Based on the OFDM signal parameters listed in Table I, the aforementioned SFO ranges for approximately ICI- and ISI-free operation are $97.66 \text{ ppm} > \delta > -97.66 \text{ ppm}$ and $48.83 \text{ ppm} > \delta > 0 \text{ ppm}$, respectively. The achieved results show that only $|\delta| \in \{100, 1000\}$ ppm among the considered normalized SFO values exceed both ICI- and ISI-free SFO ranges due to their resulting delays and frequency shifts, respectively, as previously discussed and shown in Figs. 4(b) and (c). Since the achieved ICI- and ISI-free SFO ranges do not fully cover the expected SFOs of up to ± 123 ppm that may occur in the aforementioned measurement setup that will later be considered in Section V, the SFO correction via the frequency-domain equalization from (36) is henceforth not considered and the resampling approach explained in Section III-C is adopted instead.

To clearly illustrate the effects of SFO on the receive QPSK constellation, simulation results for an AWGN channel with

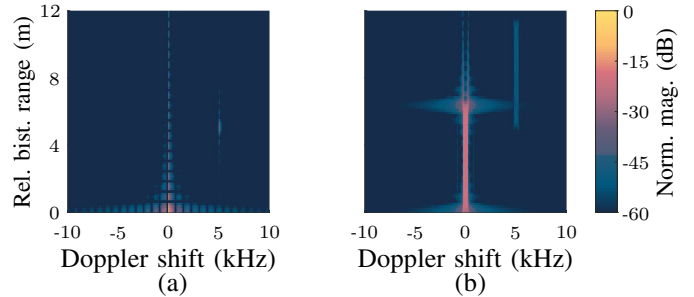


Fig. 6. Range-Doppler bistatic radar images with one reference path and a target at a relative bistatic range of 5 m and Doppler shift of 5 kHz for (a) $\delta = 0$ ppm and (b) $\delta = 1$ ppm.

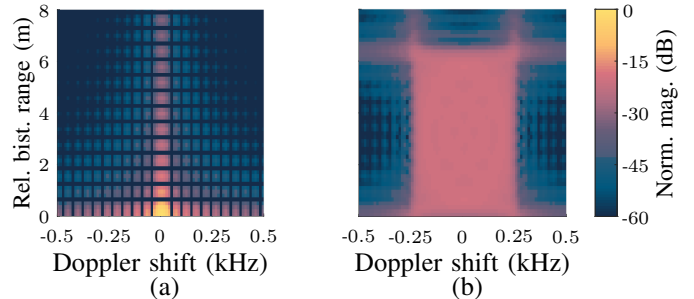


Fig. 7. Zoom-in on reference path of the radar images from Fig. 6 for (a) $\delta = 0$ ppm and (b) $\delta = 1$ ppm.

SNR = 20 dB and an SFO of $\delta = 1$ ppm are shown in Fig. 5. The assumed channel model agrees with the assumption that the reference path between transmitter and receiver is much stronger than the propagation paths associated with radar targets and that perfect time and frequency synchronization w.r.t. this main path is performed. In this aforementioned figure, the ICI effect described in (11) and shown in Fig. 4(c) can be observed for the OFDM symbol of index $m = 0$ in the form of spreading of some constellation points towards the origin, while the constellation for $m = 64$ is still clearly affected by ICI but also presents more relevant phase rotation due to the dependence of $\psi_{n,m}^{\text{SFO}}$ in (10) on the OFDM symbol index m . As for OFDM symbol $m = 4094$, both effects are

present, but the higher SFO-induced delay results in more accentuated rotation of the QPSK constellation.

Regarding sensing performance, bistatic radar images assuming $\text{SNR} = 20$ dB before radar processing and perfect time and frequency synchronization w.r.t. the reference path, as well as a radar target with $\text{SNR} = -10$ dB before radar processing, relative range of 5 m and relative Doppler shift of 5 kHz w.r.t. the main path are shown in Fig. 6 for $\delta = 0$ ppm and $\delta = 1$ ppm. In both range and Doppler shift directions, rectangular windowing was used to avoid that the SFO effects are masked by the use of a window aiming to reduce sidelobe level. For simplicity, the presented radar images are obtained by processing all subcarriers. In practice, this would require pilot-based channel estimation and equalization to correctly estimate the QPSK data in payload subcarriers and only then allow bistatic radar signal processing with the full frame as described in [16], [37]. The results in these figures show that range and Doppler shift migration occur for $\delta = 1$ ppm, spreading both the reference path and the radar target in the relative bistatic range and Doppler shift directions and reducing their magnitude and consequently SINR compared with the case with $\delta = 0$ ppm. These effects are respectively caused by delay and frequency shift migrations described by (13) and (15). A zoom in on the reference path for both cases is shown in Fig. 7. In this figure, a range migration from 0 m to $c_0\{\delta[M(N + N_{\text{CP}})]T_s\} = 6.29$ m is observed, which agrees with the expected delay migration that can be calculated based on (13). Similarly, a Doppler shift migration from $\delta(-N/2)\Delta f = -0.25$ kHz to $\delta(N/2)\Delta f = 0.25$ kHz is experienced as predicted in (14) and (15). Besides range and Doppler shift migration, both the reference path and the radar target experience SINR loss due to the SFO-induced ICI. ISI, however, is not experienced since $\delta = 1$ ppm lies in the ISI-free SFO range $48.83 \text{ ppm} > \delta > 0 \text{ ppm}$ defined by (33) for the OFDM parameterization in the considered RIS-assisted bistatic ISAC system.

The presented QPSK constellations and radar images for $\delta = 1$ ppm show that even small SFOs can greatly impair both communication and radar sensing performances of bistatic ISAC systems. For the expected SFO of up to $\delta = \pm 123$ ppm in the measurement setup later described in Section V, even higher degradation is expected since ISI can occur even for positive SFOs as indicated by Fig. 4(b). To prevent this, the experienced SFO must be accurately estimated and corrected, which is addressed in Section IV-B.

B. SFO estimation

To perform SFO estimation, the approach based on the method by Wu et al. [21], which is equivalent to the TITO method when forcing $M_{\text{pil}}^{\text{TITO}} = M_{\text{pil}}$, first estimates the delay migration, and then its slope along the pilot OFDM symbols. Only then the SFO is estimated via (21). Therefore, as discussed in Section III, the delay migration estimates must be accurate in order for an accurate SFO estimate to be obtained. In this context, the root mean squared error (RMSE) of the SFO estimates obtained with the approach based on the method by Wu et al. are shown in Fig. 8 for

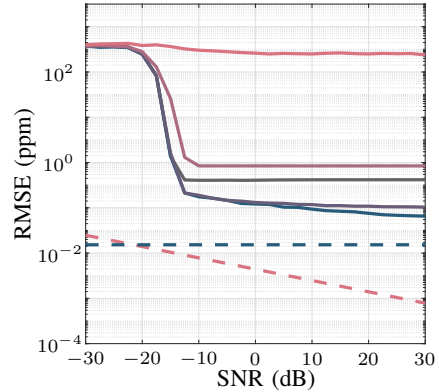


Fig. 8. RMSE of delay-based SFO estimation based on [21] for $\text{SNR} = -30$ dB through 30 dB and $\delta = 0.1$ ppm (—), $\delta = 1$ ppm (—), $\delta = 10$ ppm (—), $\delta = 100$ ppm (—), and $\delta = 1000$ ppm (—). For comparison, the approximate CRLB from (25) (---) and the lower bound for the MLE estimator with ZP from (27) (---) are also shown.

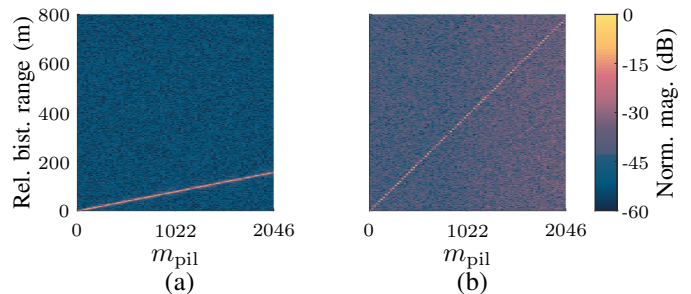


Fig. 9. Normalized delay-slow time profile assuming a reference path with $\text{SNR} = 20$ dB and a radar target with $\text{SNR} = -10$ dB at a relative bistatic range of 5 m and Doppler shift of 5 kHz for (a) $\delta = 100$ ppm and (b) $\delta = 500$ ppm. While a constant normalized magnitude ratio between the reference path and the noise floor is observed over all m_{pil} for $\delta = 100$ ppm, a smooth degradation is observed for $\delta = 500$ ppm starting at $m_{\text{pil}} \approx 1022$.

$\delta \in \{0.1, 1, 10, 100, 1000\}$ ppm. These results were obtained from the SFO estimates based on delay migration estimation with ZP factor $\eta = 20$ for $\text{SNR} = -30$ dB through 30 dB. To reduce the computational complexity associated with the high ZP factor η , chirp Z-transform (CZT) can be used instead of IDFT only around the expected reference path tap position in the columns of \mathbf{D} [47].

The obtained RMSE results show a tendency of the SFO estimates with increasing $|\delta|$. The only exception is $\delta = 0.1$ ppm, which yields worse RMSE than, e.g., $\delta = 1$ ppm and $\delta = 10$ ppm due to the limited delay estimation accuracy induced by such a low SFO. For all other SFO values, the RMSE degradation is primarily caused by the SINR reduction of the peaks corresponding to the reference path in the delay-slow time profile matrix \mathbf{D} that are used to obtain the required delay migration estimates for SFO estimation. This reduction happens due to SFO-induced ICI and ISI as discussed in Section IV-A and illustrated in Fig. 9 assuming the same SNR conditions for the reference path and the radar target as for the results in Fig. 6.

To analyze the SINR degradation more closely, the simulated SINR of the reference path estimated with each m_{pil} th pilot OFDM symbol, i.e., along the CIR esti-

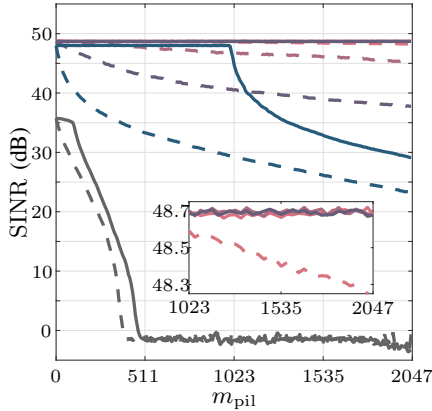


Fig. 10. SINR of the corresponding peak to the estimated reference path in the CIR estimate at the m_{pil} th column of \mathbf{D} used for obtaining the delay migration estimate $\widehat{\Delta\tau}_{\text{pil}, m_{\text{pil}}}^{\text{SFO}}$. Results are shown for $|\delta| = 0.1$ ppm (—), $|\delta| = 1$ ppm (—), $|\delta| = 10$ ppm (—), $|\delta| = 100$ ppm (—), and $|\delta| = 1000$ ppm (—), with continuous lines (—) for positive δ and dashed lines for negative δ (—).

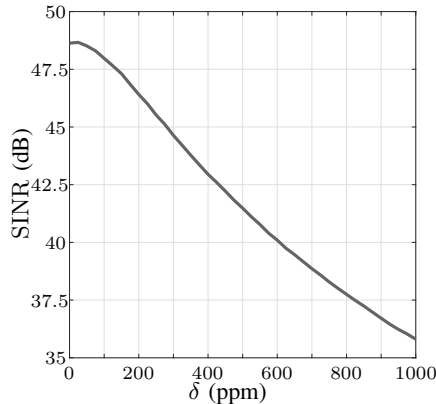


Fig. 11. SINR as a function of the SFO δ for the corresponding peak to the estimated reference path in the CIR estimate at the first column of \mathbf{D} ($m_{\text{pil}} = 0$), based on which $\widehat{\Delta\tau}_{\text{pil}, 0}^{\text{SFO}}$ is estimated.

mates in the columns of the delay-slow time profile matrix \mathbf{D} , is shown in Fig. 10 for $\text{SNR} = 20$ dB and $\delta \in \{\pm 0.1, \pm 1, \pm 10, \pm 100, \pm 1000\}$ ppm. To avoid biasing the SINR results, a Chebyshev window with 100 dB sidelobe suppression was used before forming the delay profiles at each column of \mathbf{D} , and the SINR was calculated as the ratio between the peak corresponding to the reference path and the region outside its main lobe. The obtained results show that the SINR at $m_{\text{pil}} = 0$ decreases with increasing $|\delta|$. This is solely due to the SFO-induced ICI for positive δ , since the CP prevents ISI due to delay migration at this point, and due to both SFO-induced ICI and ISI for negative δ . A relevant SINR decrease, however, is only observed for $|\delta| = 1000$ ppm among the considered δ values, while all the other SFOs result in negligible interference and therefore close SINR value to the expected SNR of 48.70 dB. This value is equal to the input SNR of 20 dB, plus the processing gain of $10 \log_{10}(N_{\text{pil}}) = 30.10$ dB, minus the windowing SNR loss of around 1.40 dB. To provide a more thorough analysis of the effect of the SFO-induced ICI, Fig. 11 shows the SINR at $m_{\text{pil}} = 0$ as a function of δ . Since, as mentioned

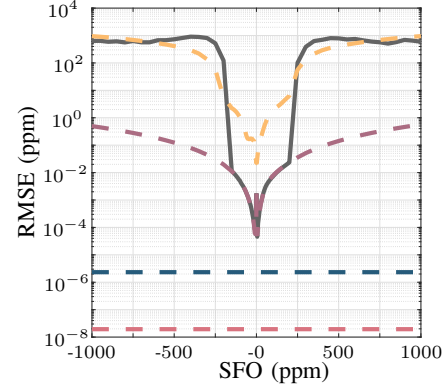


Fig. 12. RMSE of SFO estimates at $\text{SNR} = 20$ dB for $\delta = -1000$ ppm through 1000 ppm with the proposed TITO method (—), the approach based on the method by Wu et al. [21] (—), and the method by Tsai et al. [19] (—). For further comparison, the CRLB from (25) (—) and the lower bound for the MLE estimator with ZP from (27) (—) are also shown.

before, ISI already happens at $m_{\text{pil}} = 0$ for negative δ among the considered values, only positive δ is analyzed for the presented results in this figure. An SINR degradation due to SFO-induced ICI of 1 dB is only experienced at 125 ppm, which is already slightly above the maximum of 123 ppm expected in the setup later considered in Section V. Moreover, a SINR degradation of 3 dB or higher is only experienced for $\delta \geq 250$ ppm. This allows concluding that only rather high SFOs lead to significant SINR loss due to the induced ICI. Back to Fig. 10, it is observed that the SINR continuously drop for negative δ along with m_{pil} , since all OFDM symbols in the frame are affected by the aforementioned SFO-induced ISI, which becomes more severe with increasing m_{pil} as the absolute value of the delay caused by SFO from (12) increases. Under influence of positive δ , however, the SINR only starts to drop after the SFO-induced delay exceeds the CP duration, only then causing ISI.

The discussed results so far have indicated that the SFO estimates with the approach based on the method by Wu et al. may be significantly biased even without relevant influence of SFO-induced ICI when ISI eventually happens, as shown in Fig. 10. This is caused by the use of the CIR estimates in the columns of the delay-slow time profile matrix \mathbf{D} that correspond to pilot OFDM symbols of index m_{pil} that are affected by ISI. As discussed in Section III-B, this is circumvented with the TITO method by setting an upperbound to the step of the reference path delay migration between two consecutive estimates. Once this threshold is exceeded, the corresponding pilot OFDM symbol m_{pil} and all next ones are assumed to be under strong SFO-induced ISI and are therefore disregarded, leading to a total number of used pilot OFDM symbols $M_{\text{pil}}^{\text{TITO}} \leq M_{\text{pil}}$ for SFO estimation with the TITO method. Assuming $\text{SNR} = 20$ dB as in the previous analysis in this section, Fig. 12 shows the achieved RMSE of the SFO estimates with both the approach based on the method by Wu et al. and the TITO method assuming $\delta_{\text{max}} = 1000$ ppm and $\varepsilon = 0.1$ for $\delta = -1000$ ppm through $\delta = 1000$ ppm. For comparison, the performance of the method by Tsai et al. [19] is also shown. The achieved results show that, between around $\delta = -150$ ppm and $\delta = 200$ ppm, TITO yields

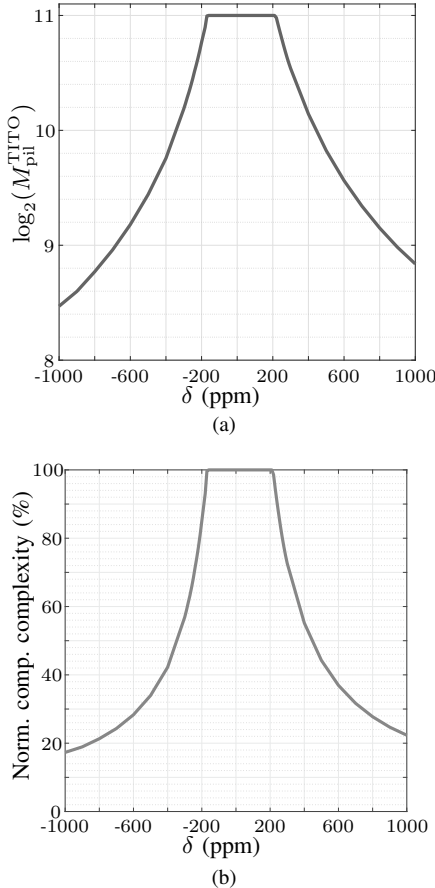


Fig. 13. Reduction in the number of used pilot OFDM symbols for SFO estimation with the TITO method at SNR = 20 dB: (a) total number M_{pil}^{TITO} of used pilot OFDM symbols as a function of the SFO δ and (b) normalized computational complexity compared with the approach based on the method by Wu et al. [21]. Between around $\delta = -150$ ppm and $\delta = 200$ ppm there is a plateau with $M_{pil}^{TITO} = M_{pil}$. For these SFO values, all pilot OFDM symbols are used for the SFO estimation with the TITO method and, consequently, no computational complexity reduction is experienced.

equivalent performance to the delay-based method based on Wu et al., while the method by Tsai et al. performs the worst. In this SFO region, the experienced processing gain of $10 \log_{10}(N_{pil}) = 30.10$ dB when analyzing the reference path in the obtained the CIR estimates stored in the columns of \mathbf{D} in the former two methods is sufficient to avoid severe degradation of the reference path SINR and consequently of the SFO estimates due to the SFO-induced ISI. The method by Tsai et al., however, does not profit from this processing gain as it operates on the subcarrier level. Outside this SFO region, the RMSE of the method based on Wu et al. is significantly worsened by the ISI-contaminated pilot OFDM symbols used to estimate the aforementioned CIRs. While the Tsai method achieves equal or better performance, it is also affected by SFO-induced ISI and its RMSE is still rather high, i.e., 5.6 ppm or more. The TITO method, in turn, circumvents the ISI issue with its choice of $M_{pil}^{TITO} \leq M_{pil}$ pilot OFDM symbols used for the delay migration estimation required to estimate the SFO as described by (35) and illustrated in Fig. 13a. In Fig. 13b, the resulting computational complexity

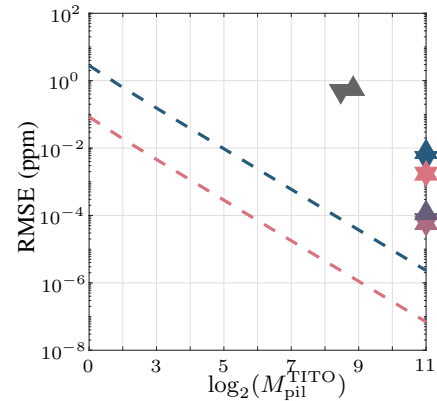


Fig. 14. RMSE of the SFO estimates at SNR = 20 dB and the total number M_{pil}^{TITO} of used pilot OFDM symbols for SFO estimation with the TITO method for $\delta = -1000$ ppm (\blacktriangledown), $\delta = -100$ ppm (\blacktriangledown), $\delta = -10$ ppm (\blacktriangledown), $\delta = -1$ ppm (\blacktriangledown), $\delta = -0.1$ ppm (\blacktriangledown), $\delta = 0.1$ ppm (\blacktriangle), $\delta = 1$ ppm (\blacktriangle), $\delta = 10$ ppm (\blacktriangle), $\delta = 100$ ppm (\blacktriangle), and $\delta = 1000$ ppm (\blacktriangle). For comparison, the CRLB from (25) (---) and the lower bound for the MLE estimator with ZP from (27) (---) as functions of M_{pil}^{TITO} are also shown.

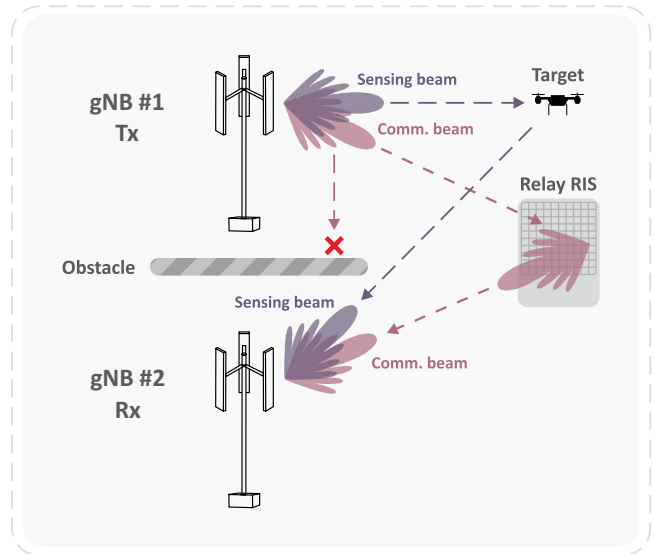


Fig. 15. RIS-assisted bistatic ISAC system concept.

experienced as less pilot OFDM symbols are processed at high SFO values is shown. The obtained results allow concluding that the performance of TITO is mainly affected by the SFO-induced ICI and the reduced number of used pilot OFDM symbols, which affects the SFO estimation accuracy as illustrated in Fig. 14. Still, TITO outperforms both its counterparts for the adopted OFDM signal parameters, presenting RMSEs as low as 0.01 ppm for $|\delta| = 150$ ppm and around 0.5 ppm for $|\delta| = 1000$ ppm.

V. MEASUREMENT SETUP AND RESULTS

In this section, the benefits of the proposed TITO method for SFO estimation and subsequent correction are demonstrated in practice. This is done via measurements based on the RIS-assisted bistatic ISAC system concept depicted in Fig. 15, which is proposed in this article to overcome NLoS conditions. In this concept, it is assumed that the LoS path between the

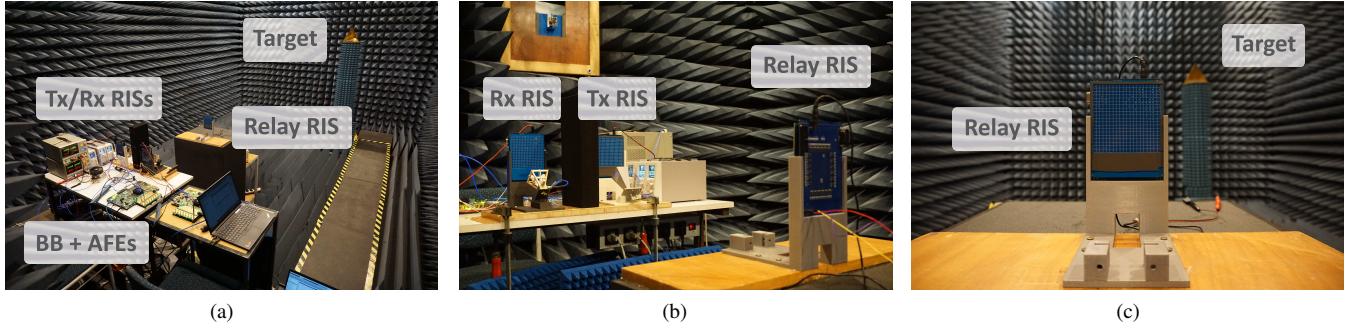


Fig. 16. Multiple views of the assembled measurement setup for the RIS-based bistatic ISAC system in the IHE anechoic chamber at the KIT.

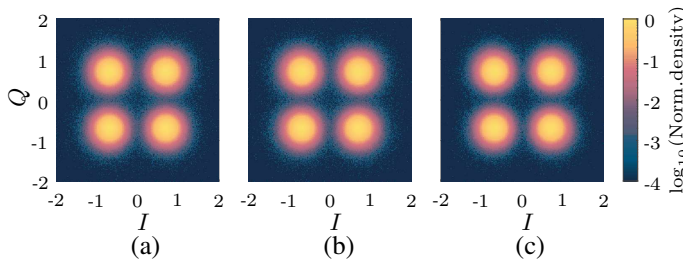


Fig. 17. Measured QPSK constellations assuming SFO estimation and correction based on (a) the method by Tsai et al. without residual SFO correction, (b) the method by Tsai et al. with residual SFO correction, and (c) the TITO method.

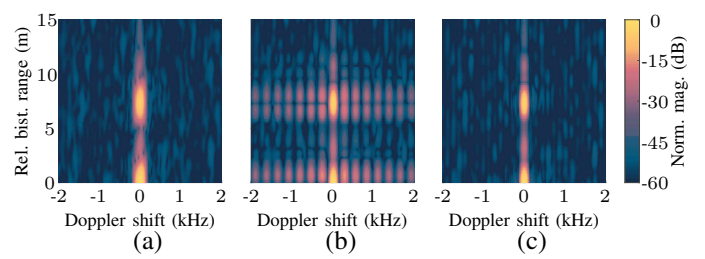


Fig. 18. Measured bistatic radar images assuming SFO estimation and correction based on (a) the method by Tsai et al. without residual SFO correction, (b) the method by Tsai et al. with residual SFO correction, and (c) the TITO method.

gNBs is obstructed, and that a relay RIS is used to steer the incoming signals from gNB #1 in the directions of gNB #2 [48].

The corresponding measurement setup to the proposed RIS-assisted bistatic ISAC system concept shown in Fig. 16 was assembled in the anechoic chamber of the Institute of Radio Frequency Engineering and Electronics (IHE) at the Karlsruhe Institute of Technology (KIT). Its BB part consisted of two Zynq UltraScale+ RFSoc ZCU111 SoC platforms from Xilinx, Inc, one acting as a transmitter and another one as a receiver. Both the transmitter and receiver boards were connected to the same RF AFEs used in [48] via coaxial cables, which then transmit/receive OFDM signals with the parameters listed in Table I to/from the transmit and receive RISs that were used as the arrays of gNB #1 and #2, respectively. Since the LoS link between transmit and receive RISs was obstructed by an RF absorber, a third RIS with known position was used as a relay. Beamforming was then performed for transmit and receive RISs so that they both had one beam pointing at the relay RISs and another beam pointing at a corner reflector placed at the other side of the anechoic chamber to serve as a radar target. While it is reasonable to assume that the beamforming directions towards the relay RIS are known, the exact beamforming directions from transmit and receive RISs towards the radar target were defined via exhaustive search. In practical deployments, more efficient approaches such as the ones from [30], [49] can be adapted to the bistatic sensing case to both perform initial target detection as mentioned in Section II.

A coordinate system was adopted for the measurement

setup shown in Fig. 16 assuming that the origin $[0, 0, 0]$ m was between the phase center of the transmitter and receiver RISs, which were located at $[-0.15, 0, 0]$ m and $[0.15, 0, 0]$ m, respectively. Furthermore, the phase center of the relay RIS was located at $[0, 1, 0]$ m and the center of the corner reflector at $[0.75, 4.50, 0.9]$ m. Considering that the reference antennas of both transmitter and receiver were located at a distance of 0.15 m of their respective RISs, the bistatic range ground truth values for the reference path enabled by the relay RIS and the radar target were 2.32 m and 9.63 m, respectively. Assuming perfect synchronization w.r.t. the reference path, this should result in a relative bistatic range of 7.31 m for the radar target.

Using the described measurement setup under the aforementioned conditions, 2 preamble OFDM symbols were transmitted before the OFDM frame to enable coarse time and frequency synchronization with the Schmidl & Cox (S&C) algorithm [33]. Afterwards, a fine time synchronization was performed via cross-correlation with the first preamble OFDM symbol to obtain a more accurate estimate of the OFDM frame start sample. After this point, SFO estimation was performed. Using the TITO method with $\delta_{\max} = 123$ ppm, which is equal to the absolute value of maximum expected SFO in the adopted setup, the same SFO estimate of -104.29 ppm was obtained as with the algorithm based on Wu et al. [21]. This was the case since only tolerable SINR degradation due to SFO-induced ICI and ISI was experienced, and therefore (35) resulted in $M_{\text{pil}}^{\text{TITO}} = M_{\text{pil}}$ pilot OFDM symbols used by the TITO method to estimate the SFO with (21), meaning that both methods are equivalent for the adopted set of parameters and hardware. Since, however, the TITO method achieves equal or better performance compared to the method based

on Wu et al. [21], the latter will be excluded from the subsequent analyses. The method by Tsai et al. [19], however, yielded a biased SFO estimate of 11.60 ppm, which ultimately resulted in a bit error ratio (BER) of 0.41 even with low-density parity-check (LDPC) decoding and produced a bistatic radar image where no targets could be detected. Out of this reason, the method by Tsai was alternatively implemented with 20 dedicated preamble OFDM symbols for SFO estimation transmitted right before the OFDM frame. Although this incurs in intolerable overhead in communication operations, only so an SFO estimate of -103.73 ppm could be obtained. Since the SFO estimation with the Tsai algorithm based on preamble symbols is not accurate enough for bistatic sensing, the latter method was also combined with a residual SFO estimation and subsequent correction via discrete-time domain shifting of the OFDM symbols as described in [16], [20]. While the aforementioned residual SFO correction compensates the delay migration, it does not alleviate the effect of the SFO-induced ICI.

After SFO estimation and correction via resampling, besides further communication processing as described in [16], [37], the QPSK constellations shown in Fig. 17 were obtained. The obtained results show virtually the same performance regardless of the SFO estimation method. This is evidenced by the error vector magnitude (EVM) with mean value of -14.84 dB and standard deviation of 5.76 dB obtained in the case where SFO estimation was performed with the TITO method, while mean EVM of -14.69 dB and standard deviation of 5.79 dB was obtained for the case where SFO estimation was done with the method by Tsai et al. without residual SFO correction and mean EVM of -14.62 dB and standard deviation of 5.79 dB for SFO estimation done with the method by Tsai et al. with residual SFO correction. In all cases, no transmission errors were experienced due to the chosen LDPC channel code [50] of rate $2/3$ and the parity check matrix for the case with 64800 bits in an LDPC code block from [51].

While the EVM performance remains virtually unaffected by the choice between the three considered SFO estimation and correction methods, the bistatic sensing performance is significantly influenced by residual SFO that lead to range and Doppler shift migrations that can be derived from delay and frequency shift migrations in (13) and (15), respectively. Fig. 18 shows the measured bistatic radar images ultimately obtained when using the aforementioned SFO estimation and correction approaches. As in [16], [37], the required full transmit frame for the bistatic radar processing was reconstructed based on the knowledge of the pilot subcarriers as well as the receive payload QPSK symbols from the constellations in Fig. 17. Furthermore, biases to the relative bistatic ranges and Doppler shifts in the radar image are removed by shifting the radar image so that the reference path, which is the stronger peak in the radar image, appears at a relative bistatic range of 0 m and Doppler shift of 0 Hz. It is observed that the bistatic radar image obtained after SFO estimation with the TITO method presents a well-defined radar target peak at a relative bistatic range of 7.19 m. In the radar image obtained after synchronization with the method by Tsai et al. without residual SFO correction, the radar target peak appears at the

same range as in the previous case and a negligible SNR loss of 0.38 dB is observed. This only happens due to the compensation of range migration via discrete-time domain shifting of the OFDM symbols in the frame. However, this comes at the cost of extra computational complexity and a significant spread in the Doppler shift direction, with multiple high sidelobes that could not be successfully suppressed by windowing. As for the case where residual SFO correction was performed after the estimation with the Tsai algorithm and resampling, a significant degradation of the range resolution and a slight degradation of the Doppler shift resolution are observed compared with the bistatic radar image obtained when the TITO method is used. In this case, the radar target peak is at a relative bistatic range of 7.34 m and a SNR loss of 2.65 dB is experienced w.r.t. the TITO case.

VI. CONCLUSION

This article introduced a novel method to perform ISI-robust SFO estimation towards robust bistatic sensing in OFDM-based ISAC systems. The proposed method, TITO, consists of using pilot OFDM subcarriers to obtain CIR estimates, from which the delay migration of a dominant, reference path with constant range is estimated. By estimating the slope of the delay migration of the reference path along consecutive CIR estimates, the SFO itself can then be estimated.

After a mathematical derivation of SFO estimation accuracy lower bounds for the cases where the delay migration estimates are performed with unbiased or MLE algorithms, the performance of the proposed TITO method for SFO estimation was verified and compared to alternative techniques in the literature. The achieved results allow concluding that TITO offers sufficiently accurate SFO estimates even for much higher SFO values that are commonly expected in practical deployments. This allows ultimately producing bistatic radar images where target reflections have higher SNR and lower sidelobe level than with the methods by Wu et al. [21] and Tsai et al. [19], enabling enabling virtually unbiased radar target parameter estimation. In addition, the computational complexity associated with the TITO algorithm is considerably reduced when compared to the its best performing competitor, i.e., the approach based on the method by Wu et al. [21], since a reduced number of pilot OFDM symbols is processed.

Considering NLoS condition between the transmitting and receiving nodes of the bistatic ISAC pair, a system concept where the aforementioned path is created by using a relay RIS was proposed. This allowed to demonstrate the performance of the TITO method in practice, showing that it achieves sufficient SFO estimation accuracy to enable communication and radar sensing in the considered bistatic ISAC system.

Although not addressed in this article, the proposed TITO method for SFO estimation can be applied with minor adjustments to bistatic ISAC systems based on alternative waveforms such as orthogonal chirp-division multiplexing and phase-modulated continuous wave [17], being combined to existing time and frequency synchronization techniques [52], [53] to enable robust communication and unbiased bistatic sensing.

REFERENCES

- [1] H. Viswanathan and P. E. Mogensen, "Communications in the 6G era," *IEEE Access*, vol. 8, pp. 57 063–57 074, Mar. 2020.
- [2] C. de Lima et al., "Convergent communication, sensing and localization in 6G systems: An overview of technologies, opportunities and challenges," *IEEE Access*, vol. 9, pp. 26 902–26 925, Jan. 2021.
- [3] T. Wild, V. Braun, and H. Viswanathan, "Joint design of communication and sensing for beyond 5G and 6G systems," *IEEE Access*, vol. 9, pp. 30 845–30 857, Feb. 2021.
- [4] F. Liu et al., "Integrated sensing and communications: Towards dual-functional wireless networks for 6G and beyond," *IEEE J. Sel. Areas Commun.*, vol. 40, no. 6, pp. 1728–1767, Jun. 2022.
- [5] S. Mandelli, M. Henninger, M. Bauhofer, and T. Wild, "Survey on integrated sensing and communication performance modeling and use cases feasibility," in *2023 2nd Int. Conf. 6G Netw.*, Oct. 2023, pp. 1–8.
- [6] A. Zhang, M. L. Rahman, X. Huang, Y. J. Guo, S. Chen, and R. W. Heath, "Perceptive mobile networks: Cellular networks with radio vision via joint communication and radar sensing," *IEEE Veh. Technol. Mag.*, vol. 16, no. 2, pp. 20–30, 2021.
- [7] A. Kadelka, G. Zimmermann, J. Plachý, and O. Holschke, "A CSP's view on opportunities and challenges of integrated communications and sensing," in *2023 IEEE 3rd Int. Symp. Joint Commun. Sens.*, Mar. 2023, pp. 1–6.
- [8] V. Shatov et al., "Joint radar and communications: Architectures, use cases, aspects of radio access, signal processing, and hardware," *IEEE Access*, pp. 1–1, 2024.
- [9] C. B. Barneto et al., "Full-duplex OFDM radar with LTE and 5G NR waveforms: Challenges, solutions, and measurements," *IEEE Trans. Microw. Theory Tech.*, vol. 67, no. 10, pp. 4042–4054, Oct. 2019.
- [10] C. B. Barneto, S. D. Liyanaarachchi, M. Heino, T. Riihonen, and M. Valkama, "Full duplex radio/radar technology: The enabler for advanced joint communication and sensing," *IEEE Wireless Commun.*, vol. 28, no. 1, pp. 82–88, Feb. 2021.
- [11] A. Książek et al., "Opportunities and limitations in radar sensing based on 5G broadband cellular networks," *IEEE Aerosp. Electron. Syst. Mag.*, vol. 38, no. 9, pp. 4–21, Sept. 2023.
- [12] R. Thomä and T. Dallmann, "Distributed ISAC systems – multisensor radio access and coordination," in *2023 20th Eur. Radar Conf.*, Sept. 2023, pp. 351–354.
- [13] M. Bauhofer, S. Mandelli, M. Henninger, T. Wild, and S. ten Brink, "Multi-target localization in multi-static integrated sensing and communication deployments," in *2023 2nd Int. Conf. 6G Netw.*, Oct. 2023, pp. 1–4.
- [14] P. Samczyński et al., "5G network-based passive radar," *IEEE Transactions on Geoscience and Remote Sensing*, vol. 60, pp. 1–9, Dec. 2022.
- [15] K. Abratkiewicz, A. Książek, M. Płotka, P. Samczyński, J. Wszolek, and T. P. Zieliński, "SSB-based signal processing for passive radar using a 5G network," *IEEE Journal Sel. Topics Appl. Earth Observations Remote Sens.*, vol. 16, pp. 3469–3484, 2023.
- [16] L. Giroto de Oliveira et al., "Bistatic OFDM-based joint radar-communication: Synchronization, data communication and sensing," in *2023 20th Eur. Radar Conf.*, Sept. 2023, pp. 359–362.
- [17] L. Giroto de Oliveira, B. Nuss, M. B. Alabd, A. Diewald, M. Pauli, and T. Zwick, "Joint radar-communication systems: Modulation schemes and system design," *IEEE Trans. Microw. Theory Tech.*, vol. 70, no. 3, pp. 1521–1551, Mar. 2022.
- [18] D. Werbunat et al., "On the synchronization of uncoupled multistatic PMCW radars," *IEEE Trans. Microw. Theory Tech. (Early Access)*, pp. 1–13, Feb. 2024.
- [19] P.-Y. Tsai, H.-Y. Kang, and T.-D. Chiu, "Joint weighted least-squares estimation of carrier-frequency offset and timing offset for OFDM systems over multipath fading channels," *IEEE Trans. Veh. Technol.*, vol. 54, no. 1, pp. 211–223, Jan. 2005.
- [20] F. Burmeister, R. Jacob, A. Traßl, N. Schwarzenberg, and G. Fettweis, "Dealing with fractional sampling time offsets for unsynchronized mobile channel measurements," *IEEE Wireless Commun. Lett.*, vol. 10, no. 12, pp. 2781–2785, Dec. 2021.
- [21] Y. Wu, Y. Zhao, and D. Li, "Sampling frequency offset estimation for pilot-aided OFDM systems in mobile environment," *Wireless Pers. Commun.*, vol. 62, pp. 215–226, Jan. 2012.
- [22] C. F. Dantas, D. Castro, and C. M. Panazio, "On enhancing the pilot-aided sampling clock offset estimation of mobile OFDM systems," *J. Commun. Inf. Sys.*, vol. 31, no. 1, pp. 108–117, Jun. 2016.
- [23] J. Pegoraro et al., "JUMP: Joint communication and sensing with unsynchronized transceivers made practical," *IEEE Trans. Wireless Commun. (Early Access)*, pp. 1–16, Feb. 2024.
- [24] C. Farrow, "A continuously variable digital delay element," in *1988 IEEE Int. Symp. Circuits Syst.*, vol. 3, Jun. 1988, pp. 2641–2645.
- [25] E. Björnson, H. Wymeersch, B. Matthiesen, P. Popovski, L. Sanguinetti, and E. de Carvalho, "Reconfigurable intelligent surfaces: A signal processing perspective with wireless applications," *IEEE Signal Process. Mag.*, vol. 39, no. 2, pp. 135–158, Mar. 2022.
- [26] S. P. Chepuri, N. Shlezinger, F. Liu, G. C. Alexandropoulos, S. Buzzi, and Y. C. Eldar, "Integrated sensing and communications with reconfigurable intelligent surfaces: From signal modeling to processing," *IEEE Signal Processing Magazine*, vol. 40, no. 6, pp. 41–62, Sept. 2023.
- [27] A. M. Elbir, K. V. Mishra, M. R. B. Shankar, and S. Chatzinotas, "The rise of intelligent reflecting surfaces in integrated sensing and communications paradigms," *IEEE Network (Early Access)*, vol. 37, no. 6, pp. 224–231, Nov. 2023.
- [28] N. J. Willis, "Bistatic radar," in *Radar Handbook*, M. I. Skolnik, Ed. New York, NY: The McGraw-Hill Companies, 2008, ch. 23, pp. 23.14–23.15.
- [29] Y. Li et al., "Realization of efficient channel estimation using programmable metasurface," in *2021 IEEE USNC-URSI Radio Sci. Meeting*, Dec. 2021, pp. 66–67.
- [30] S. Mandelli, M. Henninger, and J. Du, "Sampling and reconstructing angular domains with uniform arrays," *IEEE Trans. Wireless Commun.*, vol. 22, no. 6, pp. 3628–3642, Jun. 2023.
- [31] J. A. Zhang, X. Huang, Y. J. Guo, J. Yuan, and R. W. Heath, "Multibeam for joint communication and radar sensing using steerable analog antenna arrays," *IEEE Trans. Veh. Technol.*, vol. 68, no. 1, pp. 671–685, Jan. 2019.
- [32] S. D. Liyanaarachchi, T. Riihonen, C. B. Barneto, and M. Valkama, "Optimized waveforms for 5G–6G communication with sensing: Theory, simulations and experiments," *IEEE Trans. Wireless Commun.*, vol. 20, no. 12, pp. 8301–8315, Dec. 2021.
- [33] T. M. Schmidl and D. C. Cox, "Robust frequency and timing synchronization for OFDM," *IEEE Trans. Commun.*, vol. 45, no. 12, pp. 1613–1621, Dec. 1997.
- [34] A. Omri, M. Shaqfeh, A. Ali, and H. Alnuweiri, "Synchronization procedure in 5G NR systems," *IEEE Access*, vol. 7, pp. 41 286–41 295, Mar. 2019.
- [35] L. Smaini, "RF analog impairments description and modeling," in *RF Analog Impairments Modeling for Communication Systems Simulation: Application to OFDM-based Transceivers*. Chichester, UK: Wiley, 2012, ch. 2, pp. 37–105.
- [36] T.-D. Chiu, P.-Y. Tsai, and I.-W. Lai, "Synchronization," in *Baseband Receiver Design for Wireless MIMO-OFDM Communications, 2nd edition*. Singapore: Wiley, 2012, ch. 6, pp. 127–165.
- [37] D. Brunner et al., "Bistatic OFDM-based ISAC with over-the-air synchronization: System concept and performance analysis," *arXiv preprint arXiv:2405.04962 [eess.SP]*, May 2024.
- [38] M.-H. Hsieh and C.-H. Wei, "Channel estimation for OFDM systems based on comb-type pilot arrangement in frequency selective fading channels," *IEEE Trans. Consum. Electron.*, vol. 44, no. 1, pp. 217–225, Feb. 1998.
- [39] S. Coleri, M. Ergen, A. Puri, and A. Bahai, "Channel estimation techniques based on pilot arrangement in OFDM systems," *IEEE Trans. Broadcast.*, vol. 48, no. 3, pp. 223–229, Sept. 2002.
- [40] O. Kanhere, S. Goyal, M. Beluri, and T. S. Rappaport, "Target localization using bistatic and multistatic radar with 5G NR waveform," in *2021 IEEE 93rd Veh. Technol. Conf.*, Apr. 2021, pp. 1–7.
- [41] S. Dwivedi et al., "Positioning in 5G networks," *IEEE Commun. Mag.*, vol. 59, no. 11, pp. 38–44, Nov. 2021.
- [42] Z. Wei et al., "5G PRS-based sensing: A sensing reference signal approach for joint sensing and communication system," *IEEE Trans. Veh. Technol.*, vol. 72, no. 3, pp. 3250–3263, Mar. 2023.
- [43] M. Braun, C. Sturm, and F. K. Jondral, "On the single-target accuracy of OFDM radar algorithms," in *2011 IEEE 22nd Int. Symp. Pers., Indoor Mobile Radio Commun.*, Sept. 2011, pp. 794–798.
- [44] T. Hwang, C. Yang, G. Wu, S. Li, and G. Ye Li, "OFDM and its wireless applications: A survey," *IEEE Trans. on Veh. Technol.*, vol. 58, no. 4, pp. 1673–1694, Aug. 2009.
- [45] L. Wang, Z. Wei, L. Su, Z. Feng, H. Wu, and D. Xue, "Coherent compensation based ISAC signal processing for long-range sensing: (invited paper)," in *2023 21st Int. Symp. Model. Optim. Mobile, Ad Hoc, Wireless Netw.*, Aug. 2023, pp. 689–695.
- [46] L. Erup, F. Gardner, and R. Harris, "Interpolation in digital modems — part II: Implementation and performance," *IEEE Trans. Commun.*, vol. 41, no. 6, pp. 998–1008, Jun. 1993.

- [47] A. Bhutani, S. Marahrens, M. Gehringer, B. Göttel, M. Pauli, and T. Zwick, "The role of millimeter-waves in the distance measurement accuracy of an FMCW radar sensor," *Sensors*, vol. 19, no. 18, pp. 1–16, Sept. 2019.
- [48] Y. Li et al., "Beamsteering for 5G mobile communication using programmable metasurface," *IEEE Wireless Commun. Lett.*, vol. 10, no. 7, pp. 1542–1546, Jul. 2021.
- [49] —, "User detection in RIS-based mmWave JCAS: Concept and demonstration," *IEEE Trans. Wireless Commun. (Early Access)*, pp. 1–16, Feb. 2024.
- [50] S. Miao et al., "Trends in channel coding for 6G," *Proc. IEEE (Early Access)*, pp. 1–23, 2024.
- [51] ETSI, "Digital Video Broadcasting (DVB); Second generation framing structure, channel coding and modulation systems for Broadcasting, Interactive Services, News Gathering and other broadband satellite applications; Part 1: DVB-S2," European Telecommunications Standards Institute (ETSI), TS 302 307-1 V1.4.1, Jul. 2014.
- [52] M. de Lima Filomeno et al., "Joint channel estimation and Schmidl & Cox synchronization for OCDM-based systems," *IEEE Commun. Lett.*, vol. 26, no. 8, pp. 1878–1882, Aug. 2022.
- [53] L. Giroto de Oliveira et al., "Enabling joint radar-communication operation in shift register-based PMCW radars," in *2023 20th Eur. Radar Conf.*, Sept. 2023, pp. 85–88.